Original Article

Institution of MECHANICAL ENGINEERS
Journal of MECHANICAL ENGINEERING SCIENCE

Proc IMechE Part C:
J Mechanical Engineering Science
0(0) 1–12

DOI: 10.1177/0954406218786981
journals.sagepub.com/home/pic
SAGE

Iterative learning control with complex conjugate gradient optimization algorithm for multiaxial road durability test rig

Xiao Wang[1], Dacheng Cong[1], Zhidong Yang[1], Shengjie Xu[2] and Junwei Han[1]

Abstract

Service load replication performed on multiaxial hydraulic test rigs has been widely applied in automotive engineering for durability testing in laboratory. The frequency-domain off-line iterative learning control is used to generate the desired drive file, i.e. the input signals which drive the actuators of the test rig. During the iterations an experimentally identified linear frequency-domain system model is used. As the durability test rig and the specimen under test have a strong nonlinear behavior, a large number of iterations are needed to generate the drive file. This process will cause premature deterioration to the specimen unavoidably. In order to accelerate drive file construction, a method embedding complex conjugate gradient algorithm into the conventional off-line iterative learning control is proposed to reproduce the loading conditions. The basic principle and monotone convergence of the method is presented. The drive signal is updated according to the complex conjugate gradient and the optimal learning gain. An optimal learning gain can be obtained by an estimate loop. Finally, simulations are carried out based on the identified parameter model of a real spindle-coupled multiaxial test rig. With real-life spindle forces from the wheel force transducer in the proving ground test to be replicated, the simulation results indicate that the proposed conventional off-line iterative learning control with complex conjugate gradient algorithm allows generation of drive file more rapidly and precisely compared with the state-of-the-art off-line iterative learning control. Few have been done about the proposed method before. The new method is not limited to the durability testing and can be extended to other systems where repetitive tracking task is required.

Keywords

Service load simulation, iterative learning control, complex conjugate gradient algorithm, optimal learning gain, multiaxial road test rig

Date received: 5 January 2018; accepted: 8 June 2018

Introduction

The service load replication in laboratory has been used extensively in automotive industry. The hydraulic, multiaxial test rig is widely applied to perform the service load replication.[1] Compared with the time consuming and expensive proving ground test, the service load replication can avoid the adverse impact of reliance on driver and weather or traffic conditions but also offer better surveillance of fatigue crack. In addition, with compressed target load time histories that have been reduced in length but preserve the same damage potential as the original measured signals, it can reduce dramatically the duration time of durability testing,[1–4] especially suitable for the new vehicle development.

Nowadays, the off-line iterative learning control (ILC) is the current state-of-the-art technique in durability testing. This method was proposed by Cryer in 1976 and applied in the automotive industry.[5] In the off-line ILC, the identified linear frequency-domain system model is adopted. Usually the hydraulic test rig and the specimen under test can show strong

[1]State Key Laboratory of Robotics and System, School of Mechatronics Engineering, Harbin Institute of Technology, Harbin, China
[2]China Automotive Technology and Research Center, Tianjin, China

Corresponding author:
Zhidong Yang, State Key Laboratory of Robotics and System, School of Mechatronics Engineering, Harbin Institute of Technology, Harbin, Heilongjiang 150001, China.
Email: yangzhidong@hit.edu.cn

nonlinearity,[5] which might require the drive signal to be generated with a large amount of iterations. For sake of minimizing the premature deterioration to the specimen, accelerating the iteration convergence rate has the great significance.[6]

Lots of efforts have been undertaken by several researchers to cope with this problem from different aspects. The identified model through low-level exciting signal can be inaccurate, so more precise model can be obtained by averaging several FRF models according to the coherence function.[7] Cornelis et al.[8] utilizes the forward prediction method to adapt the linear inverse model after each iteration so as to compensate for the modeling error and to improve the convergence rate.

Time domain modeling will allow extension of the ILC approach to systems with significant nonlinearity or time-varying behavior.[5] Raath[9] introduces the state-space time domain system identification to road simulation. De Cuyper and Verhaegen[10] also adopt the state-space models to identify an industrial seat test rig and use the stable dynamic inversion to invert the obtained state-space models. The Autoregressive Moving Average Model with exogenous inputs is selected to identify a two-poster test rig.[11] Moten et al.[12] make use of adaptive inverse plant modeling technique to identify the system where the length of finite impulse response filters must be sufficient. Muller et al.[13–15] identify directly the time domain inverse model of multiaxial test rig without inverting the model like traditional method and the structure of model is optimized based on the correlation of the outputs leading to more control stability. Although parametric time model can achieve comparable accuracy with shorter measurement data, an order has to be selected for each part of the multivariable model which is onerous. Nonlinear system identification has also been investigated.[16] Xu et al.[17,18] propose a nonlinear ILC based on moving horizon model inversion to improve the computational efficiency and the inversion problem is regarded as nonlinear least squares problem solved by the constrained Gauss–Newton method. A nonlinear inverse model-based ILC is also presented to compensate the dynamics of test rig.[19] However, the nonlinear model requires numerical optimization and is still computationally infeasible for the long time signal.

Many researchers resort to combining ILC with other method to improve the convergence rate. For instance, Vaes et al.,[20] De Cuyper,[21] De Cuyper et al.[22] extend the ILC scheme with an online H_∞ feedback controller. In order to improve the controllability of test rig, Johansson and Abrahamsson[23] design a passive control loop whereby a structural component is applied to the system. Tang et al.[24] augment the off-line ILC with modified internal model to cope with the modeling error. However, it is not feasible to design a feedback controller or internal model for every component under test and the design of extra controllers is burdensome.

In order to speed up the convergence rate, ILC based on optimization has been studied as well.[25] For instance, Owens[26] and Owens et al.[27] develop the Norm Optimal ILC and Parameter Optimal ILC. In addition, the optimization techniques such as Newton method[28] and quasi-Newton method[29] have been employed to ILC. The above-mentioned optimized/optimal ILC methods are all applied to the lifted system[30] where input and output vectors are considered as discrete finite vectors. When the target signal is super-vector the scale of the system model will be huge, which can weaken the convergent rate of ILC implementation considerably.

All above researchers have promoted the generation process of drive file. To seek more suitable approach for multiaxis road test rig is still a challenge. The conjugate gradient (CG) method as an effective optimizing technique requires little storage and computation and is especially suitable for solving the large-scale nonlinear optimization problems.[31] So a new method embedding complex CG into the conventional off-line ILC (CGILC) is proposed to accelerate the acquirement of desired drive file for durability testing. The augmented CGILC combines the merit of conventional ILC and CG algorithm and is a full-automatic procedure, which does not require expert intervention.

The remainder of the paper is organized as follows. The next section describes the experimental test rig and its mathematical model. "The classical off-line ILC scheme in automotive industry" section reviews the theoretical background of the classical off-line ILC method. "The off-line ILC based on CG optimization algorithm" section presents basic mathematical theory and the principle of CGILC and analyzes the monotone convergence of the proposed method. "Simulation results and discussion" section discusses the simulation results and validates the effectiveness of the method. Finally, "Conclusion" section presents the conclusions of the paper.

In this work lower case bold letters (e.g. $\boldsymbol{u}$) and upper case bold letters (e.g. $\boldsymbol{G}$) denote vectors and matrices, respectively. In "The classical off-line ILC scheme in automotive industry" and "The off-line ILC based on CG optimization algorithm" sections the dependency of the angular frequency ω (rad/s) is omitted and time dependency functions will always be specified.

Experimental test rig description

Figure 1 shows the MTS 329 spindle-coupled test rig for suspension testing. The simulation model will be established based on mathematical theory and the data acquired from this system in order to represent the real experimental condition. By means of the approximate model, the proposed method can be

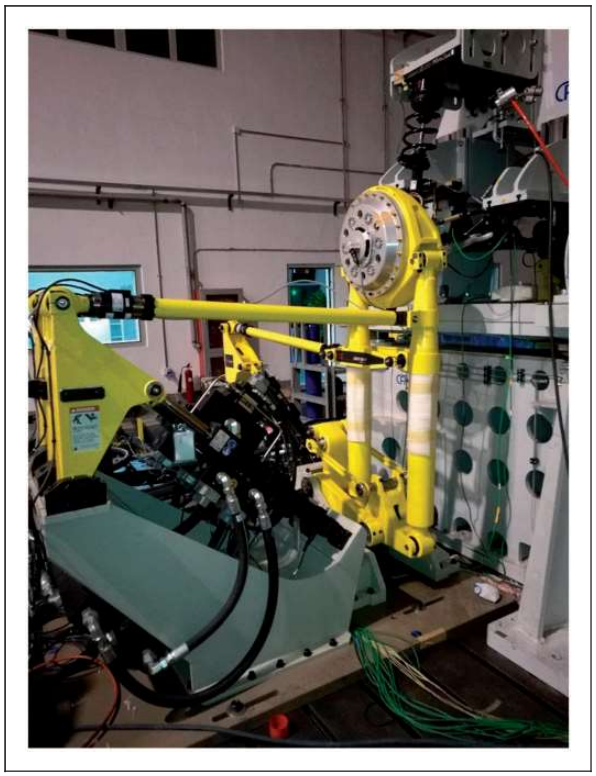

Figure 1. MTS 329 spindle-coupled test rig for suspension testing.

validated and the unexpected damage to the commercial specimen under test can also be avoided.

As shown in Figure 1, the MTS 329 6-DOF spindle-coupled test rig can reproduce the lateral, longitudinal, vertical, steer, brake, and camber movement to impose three force components and three torque components on each spindle, allowing more realistic service load replication.[21] Each six-axis mechanical movement of the test rig should have as little cross coupling as possible,[32] e.g. the unique configuration of the longitudinal and vertical channels provides a pure vertical straight-line locus at the spindle center, with minimal compensation from the longitudinal channel.

As shown in Figure 2, the system consists of a McPherson front independent suspension under test, the hydraulic test rig, and the PID controllers which control each actuator.[21]

The classical off-line ILC scheme in automotive industry

In order to analyze the control law, the desired trajectories $\boldsymbol{r}(t) = \{r_1(t), \ldots, r_N(t)\}^T$, the measured responses $\boldsymbol{y}(t) = \{y_1(t), \ldots, y_M(t)\}^T$, and the drives $\boldsymbol{u}(t) = \{u_1(t), \ldots, u_N(t)\}^T$ are transformed into the frequency domain. In the hypothesis of the system behaving linearly and being time invariant, the system can be described as

$$\boldsymbol{y} = \boldsymbol{G}\boldsymbol{u} \tag{1}$$

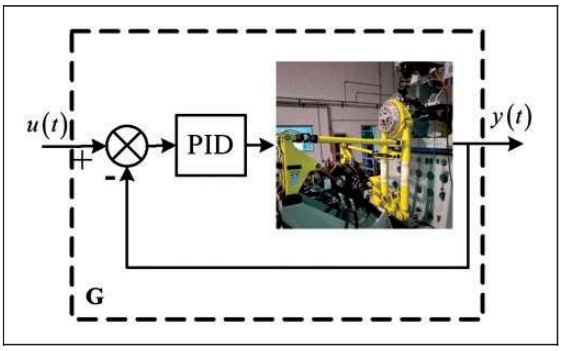

Figure 2. The control system of road test rig. PID: Proportional-Integral-Derivative controller.

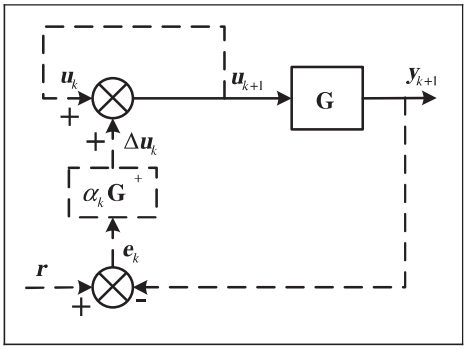

Figure 3. The classical off-line iteration control scheme.[21]

where $\boldsymbol{u} \in \mathbb{C}^{N\times 1}$ is denoted as spectra of the drive signals, $\mathbf{y} \in \mathbb{C}^{M\times 1}$ as the spectra of measured response, and $\boldsymbol{G} \in \mathbb{C}^{M\times N}$ as the frequency response function (FRF) matrix of system.

As already mentioned, the classical frequency domain iterative approach suggested by Dodds[5] is widely applied in industry for durability tests on vehicle prototypes (Figure 3). Fundamentally, this approach is comprised of two consecutive steps: system identification and drives tuning. In the identification phase, the identified experimental FRF matrix $\hat{\boldsymbol{G}}$ is typically calculated with the H_1 method.[21] Because the drive signals as inputs sent to the test rig are known exactly, the H_1 method assuming that there is no noise in the inputs is an appropriate technique to calculate the FRF matrix.[21]

Suppose the desired trajectory $\boldsymbol{r} \in \mathbb{C}^{M\times 1}$ is given, the tracking error can be expressed as

$$\boldsymbol{e} = \boldsymbol{r} - \boldsymbol{y} \tag{2}$$

The desired trajectory can be replicated completely when tracking error approximates to zero

$$\boldsymbol{r} = \boldsymbol{G}\mathbf{u}_d \tag{3}$$

where $\mathbf{u}_d$ is the optimal drive signal.

Define the mechanical impedance matrix as follows

$$\boldsymbol{Z} = \boldsymbol{G}^{+} \tag{4}$$

where the superscript + denotes the Moore–Penrose pseudo-inverse.

The drives tuning employs the identified inverse FRF matrix (the mechanical impedance matrix) to acquire the optimal drive $\mathbf{u}_d$ iteratively

$$\mathbf{u}_{k+1} = \mathbf{u}_k + \alpha_k \hat{\boldsymbol{G}}^{+} \mathbf{e}_k = \mathbf{u}_k + \alpha_k \hat{\boldsymbol{Z}} \mathbf{e}_k \quad k = 0, 1, 2, 3 \cdots \tag{5}$$

where α_k is the iteration learning gain for iteration index k, satisfying $0 \leqslant \alpha_k \leqslant 1$ and $\hat{\boldsymbol{Z}}$ is the identified mechanical impedance matrix, which can be calculated based on the singular value decomposition of $\hat{\boldsymbol{G}}$.

For specimen safety, the identification signal of the classical off-line ILC is usually low-level exciting signal. The identified linear frequency-domain model $\hat{\boldsymbol{G}}$ is utilized. The strong nonlinearity of the hydraulic test rig and the specimen under test has an adverse impact on the convergence rate of the classical off-line ILC. When a large amount of iterations are inevitable, a small learning gain α_k is adopted at the beginning and then the learning gain increases gradually with experience.

The off-line ILC based on CG optimization algorithm

The principle of ILC with optimization

Numerical iterative methods are common in computational mathematics to solve the nonlinear equations. The desired drive signal $\mathbf{u}_d$ in fact is the optimal solution of nonlinear control system inputs.[33] The control action is performed in the frequency domain, so an optimization problem over the complex space is needed to be solved.

A gradient-based technique such as the Newton's method has been extended to the complex space.[34–36] Let $\boldsymbol{z} \in \mathbb{C}^{N\times 1}$, then $\bar{\boldsymbol{z}} \triangleq \begin{bmatrix} \boldsymbol{z} \\ \boldsymbol{z}^* \end{bmatrix}$ is defined. The superscript $\cdot^*$, $\cdot^H$, and $\cdot^T$ denote the complex conjugate, the complex conjugate transpose, and the transpose, respectively. The real-valued function about $\bar{\boldsymbol{z}}$ can be represented as[35]

$$f(\bar{\boldsymbol{z}}) \triangleq f(\boldsymbol{z}, \boldsymbol{z}^*),\ \mathbb{C}^{2N} \to \mathbb{R} \tag{6}$$

The second-order Taylor expansion of $f(\bar{\boldsymbol{z}})$ can be expressed as[35]

$$f(\bar{\boldsymbol{z}} + \Delta\bar{\boldsymbol{z}}) = f(\bar{\boldsymbol{z}}) + \Delta\bar{\boldsymbol{z}}^T \frac{\partial f(\bar{\boldsymbol{z}})}{\partial \bar{\boldsymbol{z}}} + \frac{1}{2} \Delta\bar{\boldsymbol{z}}^H \frac{\partial^2 f(\bar{\boldsymbol{z}})}{\partial \bar{\boldsymbol{z}}^* \partial \bar{\boldsymbol{z}}^T} \Delta\bar{\boldsymbol{z}} \tag{7}$$

The complex gradient of equation (7) can be computed as[35]

$$\begin{aligned} \frac{\partial f(\bar{\boldsymbol{z}} + \Delta\bar{\boldsymbol{z}})}{\partial \Delta\bar{\boldsymbol{z}}^*} &= \frac{\partial f(\bar{\boldsymbol{z}})}{\partial \bar{\boldsymbol{z}}^*} + \frac{\partial^2 f(\bar{\boldsymbol{z}})}{\partial \bar{\boldsymbol{z}}^* \partial \bar{\boldsymbol{z}}^T} \Delta\bar{\boldsymbol{z}} \\ &= \nabla f(\bar{\boldsymbol{z}}) + \nabla^2 f(\bar{\boldsymbol{z}}) \Delta\bar{\boldsymbol{z}} \end{aligned} \tag{8}$$

where $\nabla f(\bar{\boldsymbol{z}})$ is the gradient and $\nabla^2 f(\bar{\boldsymbol{z}})$ is the Hessian matrix.

In order to find the minimum of equation (6), equation (8) should be equal to 0. Based on equation (8), the following expression should be satisfied[37]

$$\begin{bmatrix} \frac{\partial^2 f(\bar{\boldsymbol{z}})}{\partial \boldsymbol{z}^* \partial \boldsymbol{z}^T} & \left(\frac{\partial^2 f(\bar{\boldsymbol{z}})}{\partial \boldsymbol{z} \partial \boldsymbol{z}^T}\right)^* \\ \frac{\partial^2 f(\bar{\boldsymbol{z}})}{\partial \boldsymbol{z} \partial \boldsymbol{z}^T} & \frac{\partial^2 f(\bar{\boldsymbol{z}})}{\partial \boldsymbol{z} \partial \boldsymbol{z}^H} \end{bmatrix} \begin{bmatrix} \Delta\boldsymbol{z} \\ \Delta\boldsymbol{z}^* \end{bmatrix} = \begin{bmatrix} -\frac{\partial f(\bar{\boldsymbol{z}})}{\partial \boldsymbol{z}^*} \\ -\frac{\partial f(\bar{\boldsymbol{z}})}{\partial \boldsymbol{z}} \end{bmatrix} \tag{9}$$

Assuming $\frac{\partial^2 f(\bar{\boldsymbol{z}})}{\partial \boldsymbol{z} \partial \boldsymbol{z}^T} = 0$, then the increment $\Delta\boldsymbol{z}$ can be obtained

$$\Delta\boldsymbol{z} = -\left(\frac{\partial^2 f(\bar{\boldsymbol{z}})}{\partial \boldsymbol{z}^* \partial \boldsymbol{z}^T}\right)^{-1} \frac{\partial f(\bar{\boldsymbol{z}})}{\partial \boldsymbol{z}^*} \tag{10}$$

In MIMO control case, the Euclidean norm of error between the target and response signal is considered to be optimization function. The tracking error $\boldsymbol{e}$ will be zero at the optimum drive vectors so the assumption $\frac{\partial^2 f(\bar{\boldsymbol{z}})}{\partial \boldsymbol{z} \partial \boldsymbol{z}^T} = 0$ holds in a neighborhood of optimum vectors.[38]

Define real scalar objective function of optimization problem about the drive $\boldsymbol{u}$ as follows[39]

$$\begin{aligned} \min \Gamma(\bar{\boldsymbol{u}}) &\triangleq \Gamma(\boldsymbol{u}, \boldsymbol{u}^*) \\ &= \|\boldsymbol{e}\|^2 \\ &= (\boldsymbol{r} - \boldsymbol{G}\boldsymbol{u})^H (\boldsymbol{r} - \boldsymbol{G}\boldsymbol{u}), \mathbb{C}^{2N} \to \mathbb{R} \end{aligned} \tag{11}$$

where $\|\cdot\|$ denotes the Euclidean vector norm meaning $\|\boldsymbol{v}\| = \sqrt{\langle \boldsymbol{v}, \boldsymbol{v} \rangle} = \sqrt{\boldsymbol{v}^H \boldsymbol{v}}$, $\boldsymbol{v} \in \mathbb{C}^{N\times 1}$.

Assuming the system as linear time invariant system, the complex CG vector can be obtained

$$\nabla\Gamma = \frac{\partial \Gamma(\bar{\boldsymbol{u}})}{\partial \boldsymbol{u}^*} = -\boldsymbol{G}^H (\boldsymbol{r} - \boldsymbol{G}\boldsymbol{u}) = -\boldsymbol{G}^H \boldsymbol{e} \tag{12}$$

Subsequently, the complex Hessian matrix[40] can be derived

$$\nabla^2\Gamma = \frac{\partial^2 \Gamma(\bar{\boldsymbol{u}})}{\partial \boldsymbol{u}^* \partial \boldsymbol{u}^T} = \boldsymbol{G}^H \boldsymbol{G} \tag{13}$$

where $\boldsymbol{G}^H \boldsymbol{G}$ is positive definite Hermitian matrix for the physical system.

Based on the steepest descent method, the kth search direction $\mathbf{d}_k$ is defined as

$$\mathbf{d}_k = -\nabla\Gamma_k \tag{14}$$

And the steepest descent iteration control law is

$$\mathbf{u}_{k+1} = \mathbf{u}_k + \alpha_k \mathbf{d}_k = \mathbf{u}_k + \alpha_k \boldsymbol{G}^H \mathbf{e}_k \tag{15}$$

Considering the Newton's method, the search direction $\mathbf{d}_k$ is given by

$$\mathbf{d}_k = -\nabla^2\Gamma_k^{-1}\nabla\Gamma_k = \left(\boldsymbol{G}^H\boldsymbol{G}\right)^{-1}\boldsymbol{G}^H\mathbf{e} \tag{16}$$

The physical system model $\boldsymbol{G}$ is usually unknown so it is replaced by the identified FRF matrix $\hat{\boldsymbol{G}}$. Thus, the Newton iteration control law can be expressed as

$$\mathbf{u}_{k+1} = \mathbf{u}_k + \alpha_k\left(\hat{\boldsymbol{G}}^H\hat{\boldsymbol{G}}\right)^{-1}\hat{\boldsymbol{G}}^H\mathbf{e}_k = \mathbf{u}_k + \alpha_k\hat{\boldsymbol{G}}^+\mathbf{e}_k \tag{17}$$

The classical off-line ILC method can be deduced based on the Newton's method and can be regarded as a particular example of optimization problem. The identified FRF matrix $\hat{\boldsymbol{G}}$ is fixed and the learning gain is adjusted manually. Then, a new ILC method is proposed in the following part.

The proposed ILC based on complex CG algorithm

The method of CGs was proposed by Hestenes and Stiefel to solve the linear equation.[31] Thereafter, CG was generalized to nonlinear problems[31] by Fletcher and Reeves (FR). This method requires little storage and computation and is especially suitable for solving the large-scale nonlinear optimization problems. As a consequence, combine the classical off-line ILC with the CG algorithm in complex domain to accelerate the generation of drive file.

Applying the identified system impedance matrix, the initial drive signal is given by

$$\mathbf{u}_0 = \hat{\boldsymbol{G}}_0^+\mathbf{r} = \hat{\boldsymbol{Z}}_0\mathbf{r} \tag{18}$$

Taking the initial input as drive signal for test rig, the initial tracking error can be generated

$$\mathbf{e}_0 = \boldsymbol{r} - \boldsymbol{y}_0 = \boldsymbol{r} - \boldsymbol{G}\mathbf{u}_0 \tag{19}$$

Then, the drive signal is updated as follows

$$\mathbf{u}_{k+1} = \mathbf{u}_k + \alpha_k\mathbf{d}_k \tag{20}$$

with $\mathbf{d}_0 = -\nabla\Gamma_0 = \hat{\boldsymbol{G}}_0^H\mathbf{e}_0$.

The searching direction is updated as follows

$$\mathbf{d}_{k+1} = -\nabla\Gamma_{k+1} + \beta_k\mathbf{d}_k \tag{21}$$

The gradient can be described as

$$\nabla\Gamma_k = -\hat{\boldsymbol{G}}^H\mathbf{e}_k \tag{22}$$

The searching direction of the classical off-line iterative control is the Newton direction, which is invariant. And the CG method is the steepest descent direction, which is updated with β_k.

There are many choices about the parameter β_k in equation (21), such as FR method, Polak–Ribiere method (PR),[31] and many other variant versions. The PR method possesses a built-in restart feature that addresses the jamming problem,[35] so the PR algorithm is chosen as follows

$$\begin{aligned}\beta_{k+1} &= \frac{\mathrm{Re}\left\{\nabla\Gamma_{k+1}^H(\nabla\Gamma_{k+1} - \nabla\Gamma_k)\right\}}{\nabla\Gamma_k^H\nabla\Gamma_k} \\ &= \frac{\mathrm{Re}\left\langle\nabla\Gamma_{k+1}, \nabla\Gamma_{k+1} - \nabla\Gamma_k\right\rangle}{\langle\nabla\Gamma_k, \nabla\Gamma_k\rangle}\end{aligned} \tag{23}$$

In the classical off-line ILC, a small learning gain α_k is adopted at the beginning and then the learning gain is adjusted manually with the iterations.

In order to get the optimal iteration gain, an exact line search is performed, where the objective function is defined as

$$\begin{aligned}\min_{\alpha\in\mathbb{C}}\ \Phi(\bar{\alpha}_k) &= \Phi\left(\alpha_k, \alpha_k^*\right) \\ &= \left\|\boldsymbol{r} - \boldsymbol{G}(\mathbf{u}_k + \alpha_k\mathbf{d}_k)\right\|^2\end{aligned} \tag{24}$$

Calculate $d\Phi/d\alpha^* = 0$ to yield the learning gain

$$\alpha_k = \frac{(\boldsymbol{G}\mathbf{d}_k)^H\mathbf{e}_k}{(\boldsymbol{G}\mathbf{d}_k)^H\boldsymbol{G}\mathbf{d}_k} = \frac{\langle\boldsymbol{G}\mathbf{d}_k, \mathbf{e}_k\rangle}{\langle\boldsymbol{G}\mathbf{d}_k, \boldsymbol{G}\mathbf{d}_k\rangle} \tag{25}$$

In reality, the optimal learning gain α_k is impossible to be calculated due to unknown physical model $\boldsymbol{G}$ according to equation (25). A solution to this problem is proposed by inserting an estimating phase.[38]

In the estimating phase, the concrete procedure is shown as follows

$$\hat{\mathbf{u}}_{k+1} = \mathbf{u}_k + \lambda\mathbf{d}_k \tag{26}$$

where λ denotes the step size of estimating phase and the choice method has been investigated by many researchers,[38,41] which is defined as

$$\lambda = \frac{\left\|\hat{\boldsymbol{G}}^H\mathbf{e}_0\right\|^2}{\left\|\hat{\boldsymbol{G}}\hat{\boldsymbol{G}}^H\mathbf{e}_0\right\|^2} \tag{27}$$

Multiplying the two sides of equation (26) by $\boldsymbol{G}$ results in

$$\boldsymbol{G}\hat{\mathbf{u}}_{k+1} = \boldsymbol{G}\mathbf{u}_k + \lambda\boldsymbol{G}\mathbf{d}_k \tag{28}$$

$$\hat{\mathbf{y}}_{k+1} = \mathbf{y}_k + \lambda\boldsymbol{G}\mathbf{d}_k \tag{29}$$

Applying the two response of test rig leads to

$$\boldsymbol{G}\mathbf{d}_k = \frac{1}{\lambda}\left(\hat{\mathbf{y}}_{k+1} - \mathbf{y}_k\right) = \frac{1}{\lambda}\hat{\mathbf{e}}_k \tag{30}$$

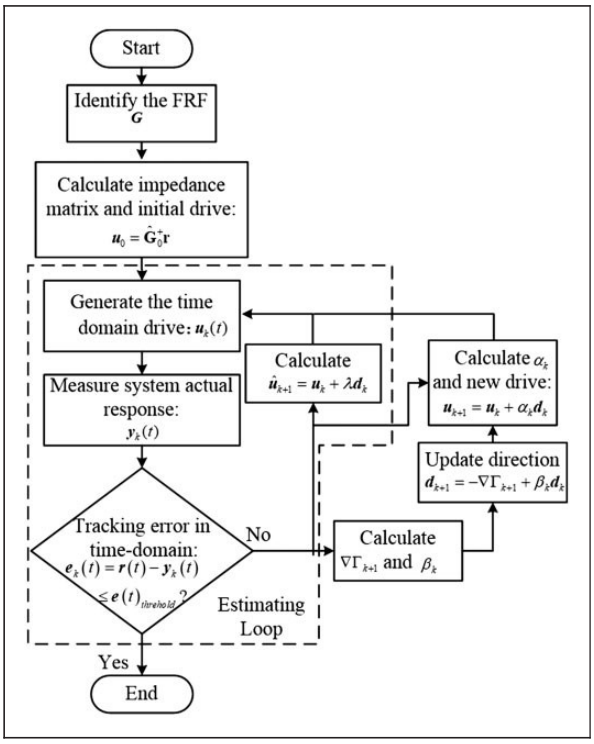

Figure 4. The flow chart of the proposed CGILC scheme. FRF: frequency response function.

Furthermore, equation (25) can be formulated as

$$\alpha_k = \lambda \frac{\langle \hat{\mathbf{e}}_k, \mathbf{e}_k \rangle}{\langle \hat{\mathbf{e}}_k, \hat{\mathbf{e}}_k \rangle} \tag{31}$$

Finally, the CGILC method is specified, of which the flow chart is exhibited in Figure 4.

Monotonic convergence of CGILC

Subsequently, a convergence analysis of the CGILC algorithm follows:

Theorem. Assume $\{\mathbf{e}_0, \mathbf{e}_1, \ldots, \mathbf{e}_{k+1}, \cdots\}$ as the tracking error sequence generated by the CGILC algorithm, then the following relation holds

$$\|\mathbf{e}_{k+1}\|^2 \leqslant \|\mathbf{e}_k\|^2 \tag{32}$$

Proof

$$\begin{aligned} \mathbf{e}_{k+1} &= \boldsymbol{r} - \boldsymbol{G}\boldsymbol{u}_{k+1} \\ &= \boldsymbol{r} - \boldsymbol{G}(\mathbf{u}_k + \alpha_k \mathbf{d}_k) \\ &= \boldsymbol{r} - \boldsymbol{G}\mathbf{u}_k - \alpha_k \boldsymbol{G}\mathbf{d}_k \\ &= \mathbf{e}_k - \alpha_k \boldsymbol{G}\mathbf{d}_k \end{aligned} \tag{33}$$

$$\begin{aligned} \|\mathbf{e}_{k+1}\|^2 - \|\mathbf{e}_k\|^2 &= -\alpha_k \langle \mathbf{e}_k, \boldsymbol{G}\mathbf{d}_k \rangle - \alpha_k^* \langle \boldsymbol{G}\mathbf{d}_k, \mathbf{e}_k \rangle \\ &\quad + \alpha_k^* \alpha_k \langle \boldsymbol{G}\mathbf{d}_k, \boldsymbol{G}\mathbf{d}_k \rangle \\ &= -\frac{\langle \boldsymbol{G}\mathbf{d}_k, \mathbf{e}_k \rangle \langle \mathbf{e}_k, \boldsymbol{G}\mathbf{d}_k \rangle}{\langle \boldsymbol{G}\mathbf{d}_k, \boldsymbol{G}\mathbf{d}_k \rangle} \\ &= -\frac{\|(\boldsymbol{G}\mathbf{d}_k)^H \mathbf{e}_k\|^2}{\|\boldsymbol{G}\mathbf{d}_k\|^2} \leqslant 0 \end{aligned} \tag{34}$$

This demonstrates that the tracking error can converge monotonically. The monotonic convergence concerns the searching direction and the optimal gain.

Simulation results and discussion

As shown in Figure 1, a McPherson front independent suspension fastened on the fixture has been tested. The front suspension is excited at the front wheel axle by vertical displacement, and lateral and longitudinal forces. The responses are the vertical, lateral, and longitudinal spindle forces measured by wheel force transducer (WFT), which results in a 3×3 system. The experimental FRF matrix of test rig is calculated with H_1 method and the identification excitation signals are low-level uncorrelated white-pink noise signals with frequency range from 0 to 50 Hz.

The magnitude and phase frequency characteristics of the longitudinal (force-to-force) FRF, lateral (force-to-force) FRF, vertical (displacement-to-force) FRF, and the coupling FRFs between different channels are shown in Figure 5(a) and (b), respectively. Figure 5 also depicts a comparison between the experimental FRF matrix $\hat{\boldsymbol{G}}$ (blue solid) and estimated FRF matrix $\tilde{\boldsymbol{G}}$ (red dotted), where the columns represent the inputs and the rows the outputs. The amplitude and phase from the $\hat{\boldsymbol{G}}_{31}$ and $\hat{\boldsymbol{G}}_{32}$ are very noisy so the coupling between vertical output and longitudinal/lateral input is small. From $\hat{\boldsymbol{G}}_{13}$ and $\hat{\boldsymbol{G}}_{23}$, the coupling between longitudinal/lateral output and vertical input is relatively large. At high frequency region of $\hat{\boldsymbol{G}}_{21}$ and $\hat{\boldsymbol{G}}_{12}$, the coupling is small.

The parameter model $\tilde{\boldsymbol{G}}$ is estimated by recursive least squares algorithm, which can be expressed as

$$\tilde{\boldsymbol{G}}_{11} = \frac{\left\{ \begin{array}{l} 4.336e{-}5z^3 + 5.515e{-}3z^2 - 1.021e - 2z \\ \quad + 5.121e - 3 \end{array} \right\}}{\left\{ \begin{array}{l} z^5 - 4.372z^4 + 7.908z^3 - 7.392z^2 \\ \quad + 3.575z - 0.7183 \end{array} \right\}} \tag{35}$$

$$\tilde{\boldsymbol{G}}_{21} = \frac{\left\{ \begin{array}{l} -0.00305z^3 + 0.009423z^2 - 0.008697z \\ \quad + 0.002325 \end{array} \right\}}{z^4 - 3.571z^3 + 4.837z^2 - 2.952z + 0.6863} \tag{36}$$

$$\tilde{\boldsymbol{G}}_{31} = \frac{\left\{ \begin{array}{l} -0.04819z^3 + 0.1155z^2 - 0.1235z \\ \quad + 0.05019 \end{array} \right\}}{\left\{ \begin{array}{l} z^5 - 1.345z^4 + 0.6594z^3 + 0.9621z^2 \\ \quad - 0.223z - 0.4349 \end{array} \right\}} \tag{37}$$

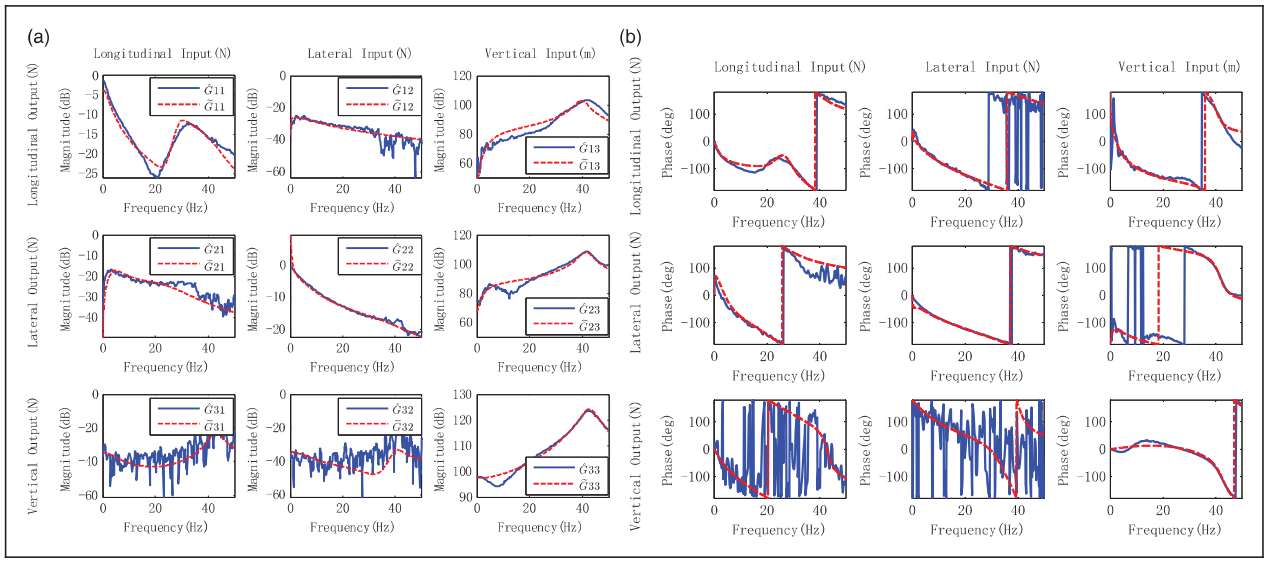

Figure 5. Experimental FRFs and identified frequency characteristics of the test rig: (a) Magnitude characteristics of system and (b) phase characteristics of system.

$$\tilde{G}_{12}=\frac{\left\{\begin{array}{l}-0.0003999z^3-0.001462z^2-0.007173z\\-0.005307\end{array}\right\}}{\left\{\begin{array}{l}z^5-2.022z^4+0.448z^3+1.567z^2\\-1.327z+0.3343\end{array}\right\}} \tag{38}$$

$$\tilde{G}_{22}=\frac{\left\{\begin{array}{l}-1.236e{-}2z^3+4.142e{-}2z^2-2.642e-2z\\-2.347e-3\end{array}\right\}}{\left\{\begin{array}{l}z^5-2.361z^4+1.065z^3+1.456z^2\\-1.633z-0.4731\end{array}\right\}} \tag{39}$$

$$\tilde{G}_{32}=\frac{\left\{\begin{array}{l}-0.01252z^3-0.0125z^2{+}0.03551z\\-0.01942\end{array}\right\}}{\left\{\begin{array}{l}z^5-1.703z^4{+}1.353z^3{+}0.832z^2\\-0.7277z-0.08502\end{array}\right\}} \tag{40}$$

$$\tilde{G}_{13}=\frac{-3469z^2{+}7010z-3541}{z^4-3.519z^3{+}4.849z^2-3.094z{+}0.7657} \tag{41}$$

$$\tilde{G}_{23}=\frac{7925z^2-27540z{+}19530}{z^4-1.618z^3-0.1095z^2{+}1.635z-0.8681} \tag{42}$$

$$\tilde{G}_{33}=\frac{2889z^2+16400z-14370}{z^4-3.061z^3+3.902z^2-2.378z+0.6038} \tag{43}$$

As can be seen from Figure 5, the estimated FRF matrix $\tilde{\boldsymbol{G}}$ matches the experimental FRF matrix $\hat{\boldsymbol{G}}$ well in most region. The order of transfer function determines the matching precision. The high-frequency

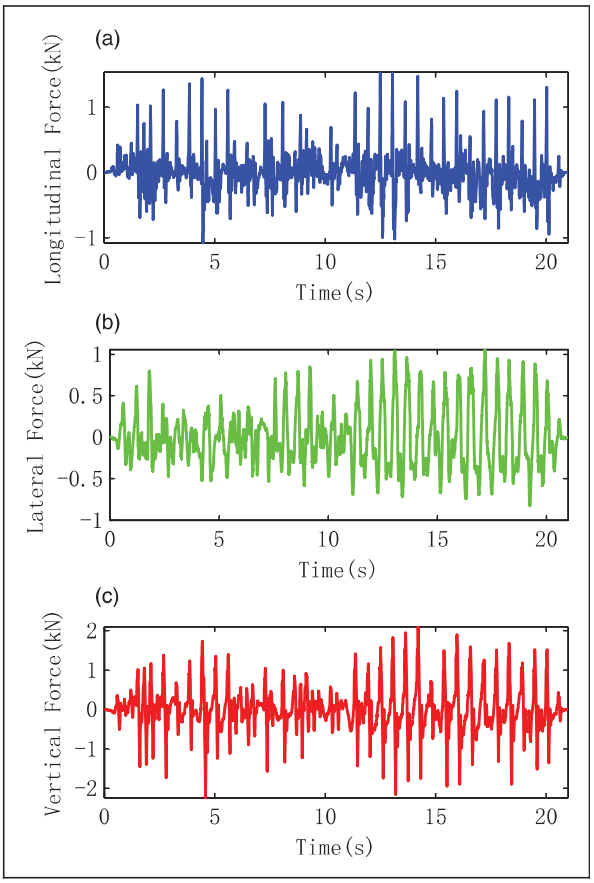

Figure 6. Time waveform of target force signal of three channels. (a) longitudinal target force, (b) lateral target force, (c) vertical target force.

dynamics needs to be represented by higher order model, which can match the physical more accurately. The choice of order of the transfer function should be trade-off between model complexity and accuracy. But it is unnecessary to match accurately because the

difference between experimental FRF matrix $\hat{\boldsymbol{G}}$ and the parameter model $\tilde{\boldsymbol{G}}$ can be regarded as the uncertainty between the identification model and the physical system.

Subsequently, the MIMO model $\tilde{\boldsymbol{G}}$ will be used to replace the physical system to verify the feasibility of the proposed CGILC algorithm in order not to jeopardize the specimen. Real-life spindle forces are measured by WFT in the proving ground test and the force responses as target signal need to be replicated. As shown in Figure 6, the force target signals of three channels all have a total length of 21 s corresponding to a rough road drive, which results in high amplitude forces.

The initial drive signal is calculated with the experimental FRF and the target force signal according to equation (18). The first excitation level is set to 20% of the initial drive signal similar to the real-life experimental operation for safety reason.

In order to quantitatively compare the convergence rate of the different methods, the relative root mean square (RMS) error of every channel is adopted and the definition is as follows

$$\varepsilon_{RMS_i} = \frac{\sqrt{\sum_{k=0}^{M} \frac{[r_i(k)-y_i(k)]^2}{M}}}{\sqrt{\sum_{k=0}^{M} \frac{r_i^2(k)}{M}}} \times 100\% \tag{44}$$

where i denotes the channel number and M is the length of the target and output signals discrete time series.

The RMS threshold of convergence is set to 1% for three channels. Figure 7 shows the relative RMS error of the classical ILC and proposed CGILC. As depicted in Figure 7, the larger gain the classical ILC has, the faster convergence rate is. In Figure 7(b), when the gain of the classical ILC is set to 0.75, lateral channel diverges because the coupling between lateral output and two other direction inputs are large. At the same time the lateral channel has little influence on the other two directions due to small coupling between lateral input and two other direction outputs. So a small gain should be set in the classical ILC to guarantee the convergence of all channels. The RMS

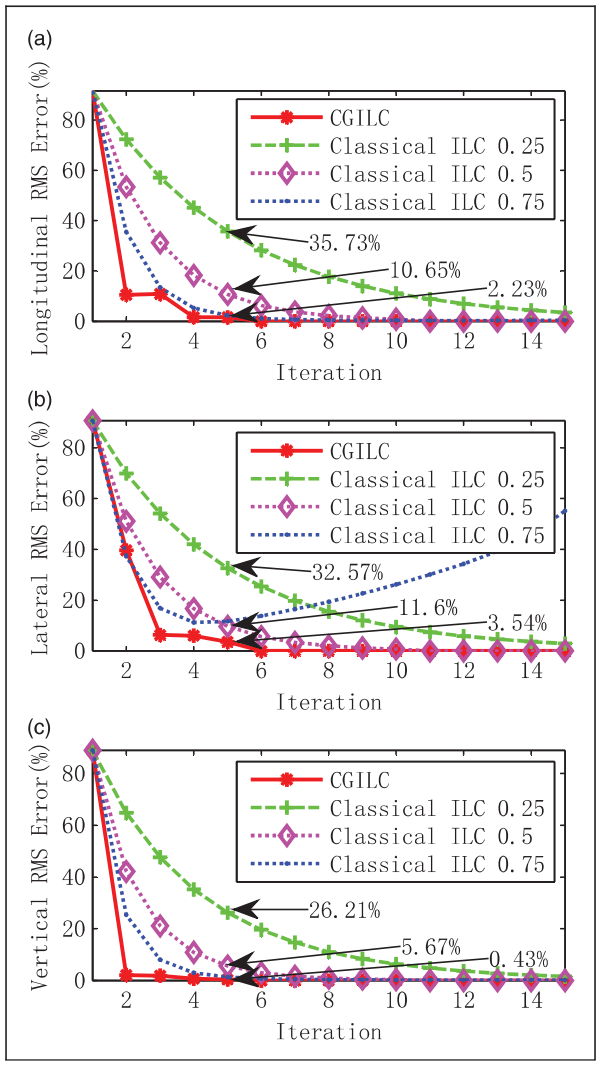

Figure 7. Relative RMS error comparison between the CGILC and the classical ILC with different gain factors. (a) longitudinal RMS error, (b) lateral RMS error, (c) vertical RMS error.
CGILC: complex CG into the conventional off-line ILC; ILC: iterative learning control.

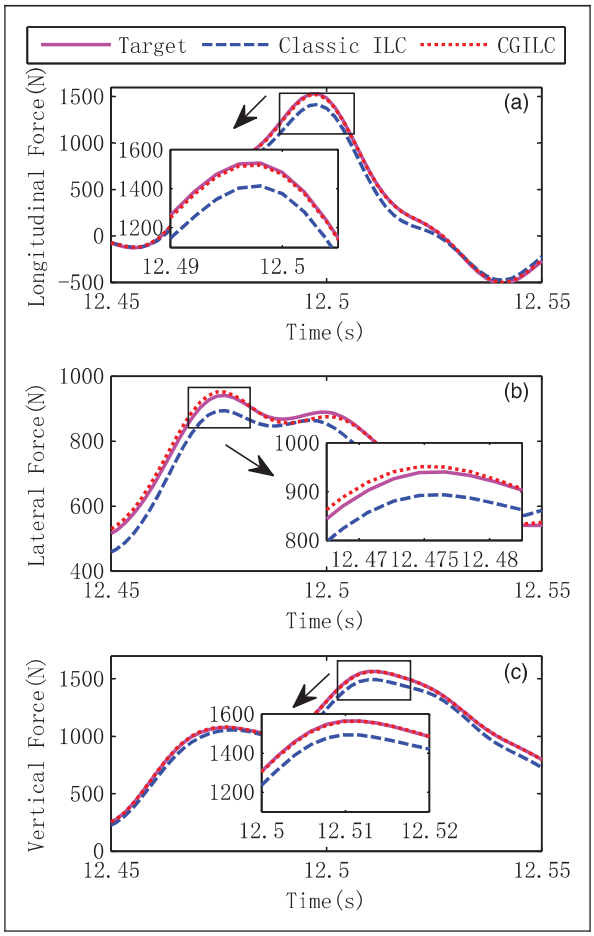

Figure 8. Time waveforms of spindle force (after five iterations). (a) longitudinal spindle force, (b) lateral spindle force, (c) vertical spindle force.
CGILC: complex CG into the conventional off-line ILC; ILC: iterative learning control.

values of the fifth iteration have been labeled in Figure 7. Obviously, it can be observed that a comparable accuracy has been reached in less iterations for the proposed CGILC although the convergence rates of three channels are different. The coupling between vertical output and longitudinal/lateral input is smallest as mentioned above so the CGILC makes vertical channel converge faster than other direction as shown in Figure 7(c). All three channels with the proposed CGILC need only six iterations to converge so it speeds up the overall process duration.

The iteration gain factor is fixed to 0.5 for the classical ILC. The time waveforms, which are obtained after five iterations with two methods, are shown in Figure 8. It can be seen that the waveforms with CGILC and target signals match better including the peak amplitude. Figure 9 exhibits tracking error after the fifth iteration. Just as discussed in Figure 7 the lateral channel is more difficult to converge due to coupling so the tracking error is higher as shown in Figure 9(b). It can be concluded from Figure 9 that more accurate results can be obtained with the CGILC with less iterations compared with the classical ILC.

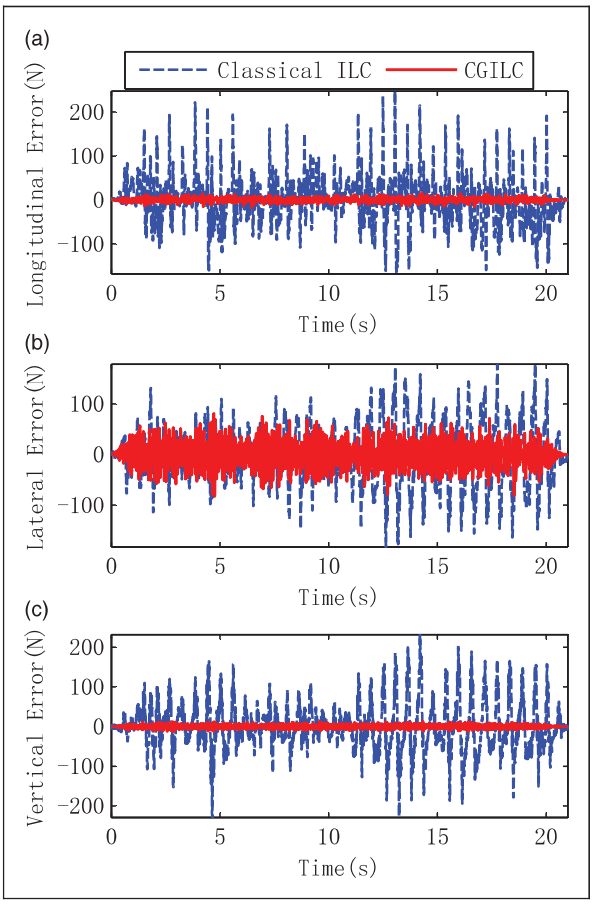

Figure 9. Tracking error comparison between the classical ILC and CGILC methods (after five iterations). (a) longitudinal tracking error, (b) lateral tracking error, (c) vertical tracking error. CGILC: complex CG into the conventional off-line ILC; ILC: iterative learning control.

Figure 10 displays the power spectral density (PSD) after the fifth iteration, respectively. It is clear that the energy is concentrated below 20 Hz and lower amplitudes occur on higher frequency. The peak PSD of three channels is located at 5 and 2 Hz, where the PSD with CGILC method matches the target better. In conclusion, the CGILC can obtain the same damage level as the target signal with less iterations.

Figure 11 compares the results of ILC and the proposed CGILC after five iterations with XY histogram. The response for one direction is plotted along the vertical axis, while the target signal for this channel is plotted along the horizontal axis. In the ideal case, when response signal is equal to the target signal,

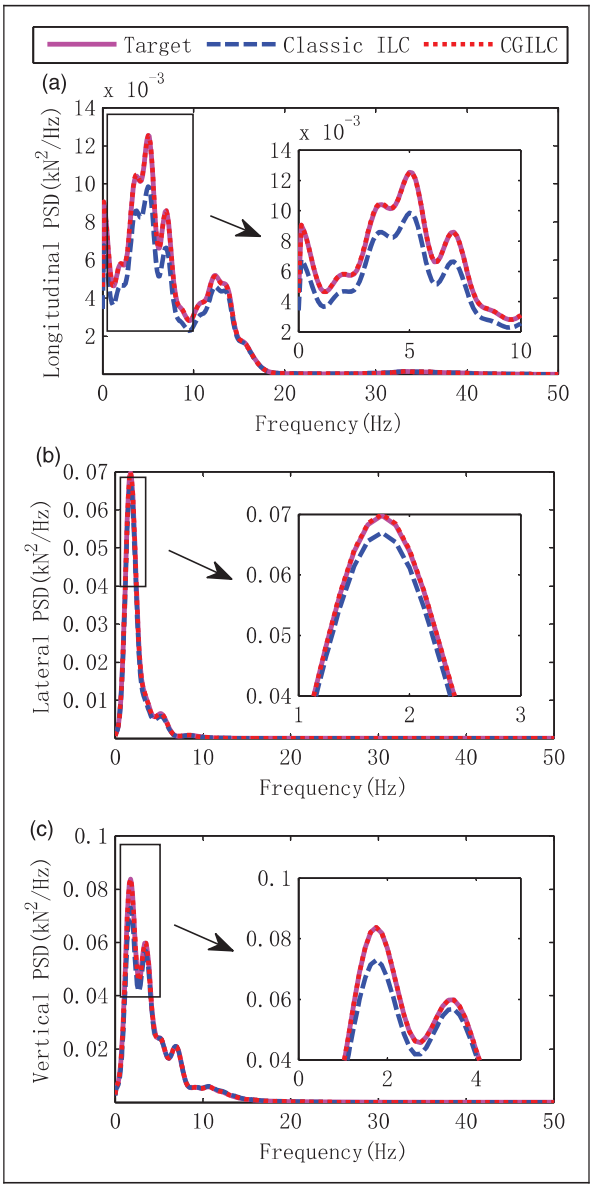

Figure 10. Power spectra of the target and the outputs simulated with the classical ILC and CGILC methods (after five iterations). (a) longitudinal PSD, (b) lateral PSD, (c) vertical PSD. CGILC: complex CG into the conventional off-line ILC; ILC: iterative learning control.

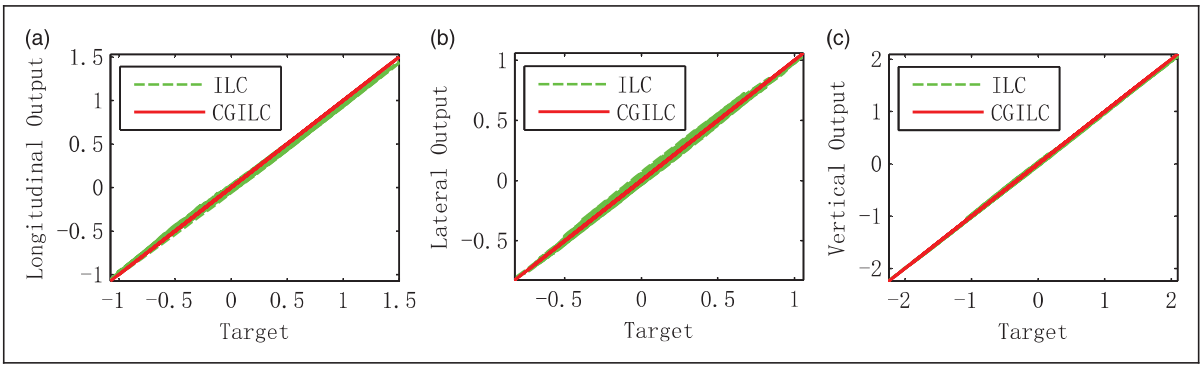

Figure 11. XY histogram between the target and the outputs simulated with the classical ILC and CGILC methods (after five iterations). (a) longitudinal XY histogram, (b) lateral XY histogram, (c) vertical XY histogram.
CGILC: complex CG into the conventional off-line ILC; ILC: iterative learning control.

the resulting plot is a straight line under 45°. The vertical outputs for both methods have more concentrated distribution than other directions. From Figure 11, it can be seen that the proposed method has better plots and the distribution is more concentrated on a straight line.

Conclusion

A new CGILC scheme is proposed to cope with the cumbersome drive signal generation process for durability test rig. This method can guarantee the tracking errors decrease monotonically. Through the estimating loop, an optimal learning gain can be acquired readily without calculating the inverse Hessian matrix of system. Simulation results reveal that a comparable accuracy can be reached in less iteration with the CGILC compared to the classical ILC, which can make a significant difference especially for the long time sequence to be replicated in automotive industry. The proposed approach toward multiple-channel implementation has been investigated through simulation. The physical multiaxial road test rig for control research is under construction and actual tests will be carried to validate the proposed procedure.

Acknowledgments

The authors would like to thank the associate editor and the reviewers for their very careful reading and valued comments, which led to the quality improvement of this paper. The authors would like to thank Guang Yang of China Automotive Technology and Research Center (CATARC) for collecting the experimental data.

Declaration of Conflicting Interests

The author(s) declared no potential conflicts of interest with respect to the research, authorship, and/or publication of this article.

Funding

The author(s) disclosed receipt of the following financial support for the research, authorship, and/or publication of this article: This research was supported by the National Natural Science Foundation of China (Grant No. 51205077).

ORCID iD

Xiao Wang http://orcid.org/0000-0002-9014-5013

References

1. De Cuyper J, Coppens D, Liefooghe C, et al. Advanced drive file development methods for improved service load simulation on multi axial durability test rigs. In: *Proceedings of the Acoustics and Vibration Asia*, 11–13 November, Singapore, 1998, pp.339–354.
2. Soderling S, Sharp M and Leser C. Servo controller compensation methods: selection of the correct technique for test applications. SAE paper 1999-01-3000, 1999.
3. Ledesma R, Jenaway L, Wang Y, et al. Development of accelerated durability tests for commercial vehicle suspension components. SAE paper 2005-01-3565, 2005.
4. Zhang H, Gui L and Fan Z. A new method to accelerate road test simulation on multi-axial test rig. SAE paper 2017-01-0200, 2017.
5. Dodds CJ and Plummer AR. Laboratory road simulation for full vehicle testing – a review. SAE paper 2001-01-0047, 2001.
6. Chindamo D, Gadola M and Marchesin FP. Reproduction of real-world road profiles on a four-poster rig for indoor vehicle chassis and suspension durability testing. *Adv Mech Eng* 2017; 9: 1–10.
7. Hu Y, Zhou H and Xu G. Study on control algorithm of the electro-hydraulic servo system for load simulation test. In: Zhang Y. (eds) *Future communication, computing, control and management*. Berlin Heidelberg: Springer, 2012, pp.533–541.
8. Cornelis B, Toso A, Verpoest W, et al. Adaptive modelling for improved control in durability test rigs. In: *Proceedings of 20th international congress on sound & vibration*, Bangkok, Thailand, 7–11 July 2013, pp.1–8. Bangkok: ICSV.
9. Raath AD. A new time domain parametric dynamic system identification approach to multiaxial service load simulation testing in components. *Int J Fatigue* 1997; 19: 409–414.
10. De Cuyper J and Verhaegen M. State space modeling and stable dynamic inversion for trajectory tracking on an industrial seat test rig. *J Vib Control* 2002; 8: 1033–1050.

11. Dursun U and Bayram T. Tracking control solution for road simulators: model-based iterative learning control approach improved by time-domain modelling. *Gazi Univ J Sci* 2012; 25: 435–446.
12. Moten S, Pipeleers G, Desmet W, et al. A combined use of the adaptive inverse plant modeling and iterative learning control strategy for service load simulations. In: *MATEC Web of Conferences*. EDP Sciences, 2016. DOI: 10.1051/matecconf/20164201002.
13. Müller T, Ziegmann J, Krüner S, et al. Optimization of inverse model identification for multi-axial test rig control. In: *MATEC Web of Conferences*. EDP Sciences, 2016. DOI: 10.1051/matecconf/20164201002.
14. Müller T, Vögele U and Endisch C. Disturbance compensation for iterative control of suspension durability test rigs. In: *2016 IEEE International Conference on Advanced Intelligent Mechatronics (AIM)*. IEEE; Banff, AB, Canada, 2016. pp.1675–1681.
15. Müller T and Endisch C. Compensation techniques for iterative rig control in multi-axial durability testing. In: *2016 IEEE 21st International Conference on Emerging Technologies and Factory Automation (ETFA)*. IEEE; Berlin, Germany, 2016. pp.1–7.
16. Volckaert M, Van Mulders A, Schoukens J, et al. Model based nonlinear iterative learning control: a constrained Gauss-Newton approach. In: *17th Mediterranean Conference on Control and Automation, 2009. MED'09*. IEEE, Thessaloniki, Greece, 2009, pp.718–723.
17. Xu G, Zhou JY and Zhou H. A new Nonlinear Iterative learning controller for road simulator. *Applied Mechanics and Materials* 2013; 373–375: 1546–1550.
18. Xu G, Volckaert M, Swevers J, et al. Moving horizon model inversion for nonlinear ILC. *Key Engineering Materials* 2011; 460–461: 184–189.
19. Eksteen JJA and Heyns PS. An alternative update formula for non-linear model-based iterative learning control. *Inverse Prob Sci Eng* 2016; 24: 860–888.
20. Vaes D, Swevers J and Sas P. Experimental validation of different MIMO-feedback controller design methods. *Control Eng Pract* 2005; 13: 1439–1451.
21. De Cuyper J. *Linear feedback control for durability test rigs in the automotive industry*. PhD Thesis, KU Leuven, Belgium, 2006.
22. De Cuyper J, Verhaegen M and Swevers J. Off-line feedforward and H∞ feedback control for improved tracking on an industrial vibration test rig. *Control Eng Pract* 2003; 11: 129–140.
23. Johansson A and Abrahamsson T. An experimental approach to improve controllability in test rigs using passive components. In: *Proceedings of the 2012 International Seminar on Modal Analysis (ISMA 2012)*, Leuven, Belgium, 17–19 September 2012, pp.2367–2381. Leuven: ISMA.
24. Tang Y, Shen G, Zhu ZC, et al. Time waveform replication for electro-hydraulic shaking table incorporating off-line iterative learning control and modified internal model control. *Proc IMechE, Part I: J Systems and Control Engineering* 2014; 228: 722–733.
25. Ge X, Stein JL, Ersal T. Frequency-domain analysis of robust monotonic convergence of norm-optimal iterative learning control. *IEEE Transactions on Control Systems Technology* 2018; 26: 637–651.
26. Owens DH. Multivariable norm optimal and parameter optimal iterative learning control: a unified formulation. *Int J Control* 2012; 85: 1010–1025.
27. Owens DH, Chu B and Mutita S. Parameter-optimal iterative learning control using polynomial representations of the inverse plant. *Int J Control* 2012; 85: 533–544.
28. Owens DH. Monotonic Newton method based ILC with parameter optimization for non-linear systems. *Int J Control* 2007; 80: 1291–1298.
29. Xu G, Shao C, Han Y, et al. New quasi-Newton iterative learning control scheme based on rank-one update for nonlinear systems. *J Supercomput* 2014; 67: 653–670.
30. Dijkstra BG and Bosgra OH. Extrapolation of optimal lifted system ILC solution, with application to a waferstage. In: *American Control Conference, 2002. Proceedings of the 2002*. IEEE, Anchorage, AK, USA, 2002, pp.2595–2600.
31. Nocedal J and Wright SJ. Conjugate gradient methods. *Numerical Optimization* 2006; 101–134.
32. Kim JW, Xuan DJ and Kim YB. Robust control application for a three-axis road simulator. *J Mech Sci Technol* 2011; 25: 221–231.
33. Hay NC and Roberts DE. Road simulators: the iterative algorithm for drive file creation. SAE paper 2006-01-0731, 2006.
34. Brandwood DH. A complex gradient operator and its application in adaptive array theory. In: *IEE Proceedings F-Communications, Radar and Signal Processing*. IET. Vol. 130, 1983, pp.11–16.
35. Sorber L, Barel MV and Lathauwer LD. Unconstrained optimization of real functions in complex variables. *SIAM J Optim* 2012; 22: 879–898.
36. Musella U, Manzato S, Peeters B, et al. CR-Calculus and adaptive array theory applied to MIMO random vibration control tests. *Journal of Physics: Conference Series* 2016; 744: 12175. DOI: 10.1088/1742-6596/744/1/012175.
37. Li H and Adali T. Optimization in the complex domain for nonlinear adaptive filtering. In: *2006 Fortieth Asilomar Conference on Signals, Systems and Computers*. IEEE, Pacific Grove, CA, USA, 2006, pp.263–267.
38. Underwood MA. *Adaptive control method for multi-exciter sine tests*. Patent 5299459, USA, 1994.
39. Jacobs DAH. A generalization of the conjugate-gradient method to solve complex systems. *IMA J Num Anal* 1986; 6: 447–452.
40. Van Den Bos A. Complex gradient and Hessian. *IEE Proceedings-Vision, Image and Signal Processing* 1994; 141: 380–382.
41. Owens DH, Hätönen JJ and Daley S. Robust monotone gradient-based discrete-time iterative learning control. *Int J Rob Nonlinear Control* 2009; 19: 634–661.

Appendix

Notation

$\mathbb{C}$	complex number space
$\mathbf{d}$	iteration direction vector
e	tracking error in frequency domain
$\hat{\mathbf{e}}$	tracking error of learning loop
G	FRF matrix of system
G^{+}	Moore–Penrose pseudo-inverse
$\hat{G}$	experimental FRF matrix
$\tilde{G}$	estimated parameter model
r	desired trajectory in frequency domain
$r(t)$	desired trajectory in time domain
$\mathbb{R}$	real number space
u	drive signal in frequency domain
$\hat{\mathbf{u}}$	drive signal of learning loop
$u(t)$	drive signal in time domain
$\mathbf{u}_d$	optimal drive signal
y	response in frequency domain
$y(t)$	response in time domain
$\hat{\mathbf{y}}$	response of learning loop
z	complex number
Z	mechanical impedance matrix
$\hat{Z}$	identified mechanical impedance matrix
α_k	iteration gain
β	iteration step size of conjugate gradient algorithm
ε_{RMS_i}	relative RMS error
λ	step size of learning loop
ω	angular frequency